Constraining Properties of Dark Matter particles Using Astrophysical Data

Iakubovskyi, D.

Cover Page

The handle http://hdl.handle.net/1887/20523 holds various files of this Leiden University dissertation.

Author: Iakubovskyi, Dmytro
Title: Constraining properties of dark matter particles using astrophysical data
Issue Date: 2013-02-13

Chapter 4

Detection strategy

The results of the previous Chapter demonstrate that the decaying dark matter would provide a unique all-sky signal, with a known slow-varying angular distribution, correlated with the matter distribution in the local Universe. Therefore *(a)* without sacrificing the expected signal one has a freedom of choosing observational targets, avoiding complicated astrophysical backgrounds; *(b)* if a candidate line is found, its surface brightness profile may be measured (as it does not decay quickly away from the centers of the objects) and distinguished from astrophysical lines that usually decay in outskirts of galaxies and clusters. Moreover, any tentative detection in one object would imply a signal of certain (comparable) signal-to-noise ratio from a number of other objects. This can be checked and the signal can either be unambiguously confirmed to be that of dark matter decay origin or ruled out. This allows to distinguish the decaying dark matter line from any possible astrophysical background and therefore makes astrophysical search for the decaying dark matter *another type of a direct detection experiment*.

In Sec. 4.1 we demonstrate the power of this approach. We check the claim of Ref. [316], that a spectral feature at 2.51 ± 0.07 keV in the spectrum of the Milky Way satellite known as Willman 1 [317]. By assuming that the reported signal comes from a dark matter decay line, we predict the parameters of corresponding decaying dark matter line in several local galaxies. After careful analysis of available X-ray observations of these objects, we find no significant line-like emission at ~ 2.5 keV range, which allows us to exclude the dark matter origin of this spectral feature at $\gtrsim 14\sigma$ level.

Then, we summarize all existing bounds on decaying dark matter lifetime

in the keV energy range in Sec. 4.2. These results are obtained from the analysis of medium exposure (about 100 kilo-seconds) X-ray observations of individual objects of different types. In Section 4.3 we discuss the best observational targets and possible ways to improve the existing bounds and probe the theoretically interesting regions of particle physics models.

We conclude that a combination of hundreds of archival observations of nearby galaxies, uniformly processed should in principle allow to increase the sensitivity for weak lines *and* study spatial dependence of each candidate line.

4.1 Verification of the dark matter origin of a spectral feature

A spectral feature at 2.51 ± 0.07 keV with the ux $(3.53\pm1.95)\times10^{-6}$ cts cm^{-2}s^{-1} (all errors at 68% confidence level) in the spectrum of Willman 1 was proposed in [316] as a candidate for a dark matter decay line. According to [316], the line with such parameters is marginally consistent the restrictions on decaying dark matter from some objects (see e.g. [318, 319] or the restrictions from the 7 ks observation of Ursa Minor dwarf spheroidal in [228]). The results of other works (e.g. [225, 227, 230]) are inconsistent at 3σ level with having 100% of decaying dark matter with the best-fit parameters of [316]. However, it is hard to exclude completely new unknown systematic uncertainties in the dark matter mass estimates and therefore in expected signal, from any given object. To this end, in this work we explicitly check for a presence of a line with parameters, specified above, by using archival observations by *XMM-Newton* of several objects, where comparable or stronger signal was expected. We compare the signals from several objects and show that the spatial (angular) behavior of the spectral feature is inconsistent with its dark matter origin so strongly, that systematic uncertainties cannot affect this conclusion. We also discuss a possible origin of the spectral feature of [316].

4.1.1 Choice of observational targets

Willman 1 signal. In [316] the signal was extracted from the central $5'$ of the Willman 1 observation. Assuming the dark matter origin of this sig-

nal, the observed flux $(3.53 \pm 1.95) \times 10^{-6}$ photons cm^{-2}s^{-1} corresponds to $F_{\mathrm{W1}} = (4.50 \pm 2.5) \times 10^{-8}$ photons cm^{-2}s^{-1}arcmin^{-2} flux per unit solid angle. The mass within the field-of-view (FoV) of the observation of Willman 1 was estimated in [316] to be $M_{\mathrm{W1}}^{\mathrm{fov}} = 2 \times 10^6 M_\odot$, using the best-fit values from [191]. Taking the luminous distance to the object to be $D_L = 38\,\mathrm{kpc}$, the average dark matter column density of Willman 1 is $\mathcal{S}_{\mathrm{W1}} \simeq 208.5\ M_\odot\ \mathrm{pc}^{-2}$ (see however discussion in the Section 4.1.4 below). To check the presence of a dark matter decay line, we should look for targets with comparable signal.

The signal-to-noise ratio for a weak line observed against a featureless continuum is given by (see e.g. discussion in [229]):

$$(S/N) \propto \mathcal{S}\sqrt{t_{\mathrm{exp}} A_{\mathrm{eff}} \Omega_{\mathrm{fov}} \Delta E} \qquad (4.1)$$

where $\mathcal{S}$ is the average dark matter column density within an instrument's field-of-view Ω_{fov}, t_{exp} is the exposure time, A_{eff} is an effective area of the detector and ΔE is the spectral resolution (notice that the line in question has a much smaller intrinsic width than the spectral resolution of *Chandra* and *XMM-Newton*). For the purpose of our estimate we consider the effective areas of *XMM-Newton* MOS cameras and *Chandra* ACIS-I (as well as their spectral resolutions) to be approximately equal, and effective area of PN camera is 2 times bigger, see Sec. 3.2.2 of [320] and [321].

Galactic contribution. The contribution of the Milky Way's dark matter halo along the line of sight should also be taken into account, when estimating the dark matter decay signal[1]. Using a pseudo-isothermal profile

$$\rho_{\mathrm{iso}}(r) = \frac{\rho_c}{1 + r^2/r_c^2}, \qquad (4.2)$$

with parameters, adopted in [223, 228] ($r_c = 4\,\mathrm{kpc}$, $\rho_c = 33.5 \times 10^6 M_\odot/\,\mathrm{kpc}^3$, $r_\odot = 8\,\mathrm{kpc}$), the corresponding Milky Way column density in the direction of Willman 1 (120.7° off Galactic center) is $73.9 M_\odot\ \mathrm{pc}^{-2}$. As demonstrated in [231], the value of dark matter column density computed with this dark matter density profile coincides with the best-fit Navarro-Frenk-White [305, **NFW**] profiles of [194] and [195] within few % for the off-center angle $\phi \gtrsim 90°$. Other dark matter distributions produce systematically larger values of dark matter column density. For example, the best-fit pseudo-isothermal profile of [322] would corresponds to an additional Milky Way contribution

---

[1]Notice, that both in [316] and in this work only instrumental (particle) background has been subtracted from the observed diffuse spectra.
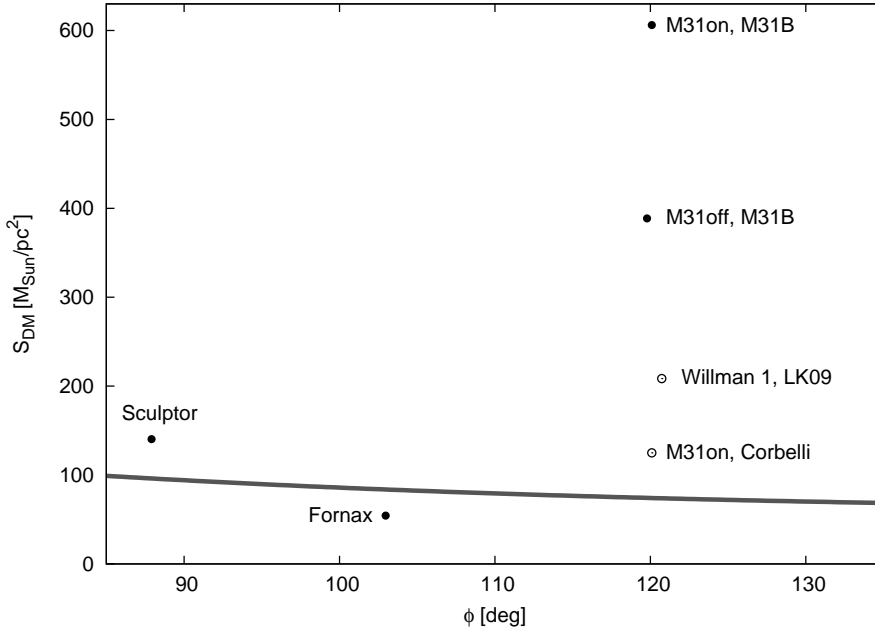
Figure 4.1: Comparison of dark matter column densities of the Milky Way (grey solid line) with the density profiles of M31, Fornax and Sculptor dSphs, discussed in the text. The dark matter column density estimate for Willman 1 is based on the "optimistic" dark matter density profile from [191], used in [316] (see [323] for discussion). The angle ϕ marks the direction off Galactic center (for an object with galactic coordinates (l, b) $\cos \phi = \cos l \cos b$).

$\sim 119 M_\odot \text{ pc}^{-2}$ in the direction of Willman 1. The comparison between the dark matter column densities of several objects with that of Milky Way in their directions is shown in Fig. 4.1.

4.1.2 *XMM-Newton* data analysis

For each *XMM-Newton* observation observation, we extracted both EPIC MOS and PN spectra.[2] According to standard recipies of *XMM-Newton* EPIC data analysis, we select only good events produced by photons from neighbouring pixels (for MOS cameras) and single pixel (for PN camera). We used the standard SAS task edetect_chain to exclude point sources, detected

---

[2]We use SAS version 9.0.0 and XSPEC 12.6.0.

with the likelihood values above 10 (about 4σ). For EPIC PN camera, bright strips with out-of-time events were also filtered out, following the standard procedure [324]. We imposed stringent flare screening criteria. To identify "good time intervals" we performed a light-curve cleaning, by analyzing temporal variability in the hard ($E > 10$ keV) X-ray band (as described e.g. in [325–327]). The resulting light curves were inspected "by eye" and additional screening of soft proton flares was performed by employing a method similar to that described in e.g. [328, 329] (i.e. by rejecting periods when the count rate deviated from a constant by more than 2σ). The extracted spectra were checked for the presence of residual soft proton contaminants by comparing count rates in and out of field-of-view [328, 330].[3] In all spectra that we extracted the ratio of count rates in and out of field-of-view did not exceed 1.13 which indicates thorough soft proton flare cleaning (c.f. [328]).

Following the procedure, described in [327] we extracted the filter-wheel closed background [332] from the same region as signal (in detector coordinates). The background was further renormalized based on the $E > 10$ keV band count rates of the extracted spectra. The resulting source and background spectra are grouped by at least 50 counts per bin using FTOOL [333] command `grppha`.

The extracted spectra with subtracted instrumental background were fitted by the `powerlaw` model of XSPEC in the energy range 2.1–8.0 keV data for MOS and 2.1–7.2 keV for the PN camera. This choice of the *baseline model* is justified by the fact that for all considered objects we expect no intrinsic X-ray emission above 2 keV and therefore the observed signal is dominated by the extragalactic diffuse X-ray background (XRB) with the power-law slope $\Gamma = 1.41 \pm 0.06$ and the normalization $(9.8 \pm 1.0) \times 10^{-7}$ photons cm^{-2} s^{-1} keV^{-1} arcmin^{-2} at 1 keV (90% confidence range errors) (see e.g. [326, 327, 330, 334–336]). Galactic contribution (both in absorption and emission) is negligible at these energies and we do not take it into account in what follows. For all considered observations `powerlaw` model provided a very good fit, fully consistent with the above measurements of XRB. The `powerlaw` index was fixed to be the same for all cameras (MOS1, MOS2, PN), observing the same spatial region, while the normalization was allowed to vary independently to account for the possible off-axis calibration uncertainties

---

[3]We use the public script [331] provided by the *XMM-Newton* EPIC Background working group and described in [330].

ObsID	PL index	PL norm, 10^{-4}ph. cm^{-2} s^{-1} keV^{-1}) at 1 keV (MOS1 / MOS2 / PN)	χ^2/dof
M31on observations:			
0109270101	1.33	5.71 / 5.80 / 7.88	1328/1363
0112570101	...	5.37 / 6.12 / 6.86	...
0112570401	...	6.13 / 6.66 / 6.37	...
M31off observation:			
0402560301	1.46	6.28 / 6.12 / 9.97	895/997
M31out observations:			
0511380101	1.53	2.75 / 2.88 / 3.89	875/857
0109270401	1.47	5.02 / 4.41 / 5.22	606/605
0505760401	1.27	1.91 / 2.04 / 2.47	548/528
0505760501	1.28	2.25 / 1.85 / 3.03	533/506
0402561301	1.57	2.94 / 3.10 / 3.95	489/515
0402561401	1.47	4.33 / 3.58 / 4.47	751/730
0402560801	1.55	5.22 / 4.49 / 5.83	902/868
0402561501	1.44	2.70 / 4.29 / 6.67	814/839
0109270301	1.39	4.29 / 4.58 / 3.75	413/436
Fornax observation:			
0302500101	1.52	4.46 / 4.02 / 3.78	938/981

Table 4.1: Best-fit values of `powerlaw` index and normalization for each *XMM-Newton* observation analyzed in this paper. The systematic uncertainty is included (see text). In M31on region, `powerlaw` index for different observations is chosen to be the same, because they point to the same spatial region.

between the different cameras, see e.g. [337, 338]. The best-fit values of the `powerlaw` index and normalizations are presented in Table 4.1.

To check for the presence of the [316] line in the spectra, we added a narrow ($\Delta E/E \sim 10^{-3}$) Gaussian line (XSPEC model `gaussian`) to the baseline `powerlaw` model. Assuming the dark matter origin of this line, we fix its normalization at the level F_{W1}, derived in [316], multiplied by the ratio of total (including Milky Way contribution) dark matter column densities and instrument's field-of-view. We vary the position of the line in the interval corresponding to the 3σ interval of [316]: $2.30 - 2.72$ keV. Eq. (4.1) allows to estimate the expected significance of the line.

When searching for weak lines, one should also take into account uncertainties arising from the inaccuracies in the calibration of the detector response and gain. This can lead to systematic residuals caused by calibration inaccuracies, at the level $\sim 5\%$ of the model flux (some of them having edge-like or even line-like shapes) [see e.g. 339, 340] as well as discussion in [226] for similar uncertainties in *Chandra*. To account for these uncertainties we perform the above procedure with the 5% of the model flux added as a systematic error (using XSPEC command systematic).

4.1.3   Andromeda galaxy

4.1.3.1   Dark matter content of M31

The Andromeda galaxy is the closest spiral galaxy to the Milky Way. Its dark matter content has been extensively studied over the years [see e.g. 11, 12, 194, 197, 285, 298, 322, and references therein] for an incomplete list of recent works. The total dynamical mass (out to ~ 40 kpc) can be determined from the rotation curve measured from H I kinematics. The major uncertainty in determination of dark matter content is then related to a separation of contributions of baryonic (stellar bulge and especially, extended stellar disk) and dark components to the total mass.[4] The baryonic mass is often obtained from the (deprojected) surface brightness profile (optical or infrared), assuming certain mass-to-light ratio for the luminous matter in the bulge and the disk of a galaxy.

[230] analyzed dark matter distributions of M31, existing in the literature at that time in order to provide the most conservative estimate of the expected dark matter decay signal. The dark matter column density $\mathcal{S}$ in more than 10 models from the works [194, 197, 285, 298, 322] turns out to be consistent within a factor of ~ 2 for off-center distances greater than ~ 1 kpc (see gray lines in Fig. 4.2). The most conservative estimate of dark matter column density was provided by one of the models of [197] (called in that work M31B), marked as thick solid line on Fig. 4.2.

Recently two new H I surveys of the disk of M31 were performed [11, 12]

---

[4]Some works also take into account a presence of supermassive black hole in the center of a galaxy [see e.g 197] and additional contribution of a gaseous disk [c.f. 11, 12]. Their relative contributions to the mass at distances of interest turn out to be negligible and we do not discuss them in what follows.
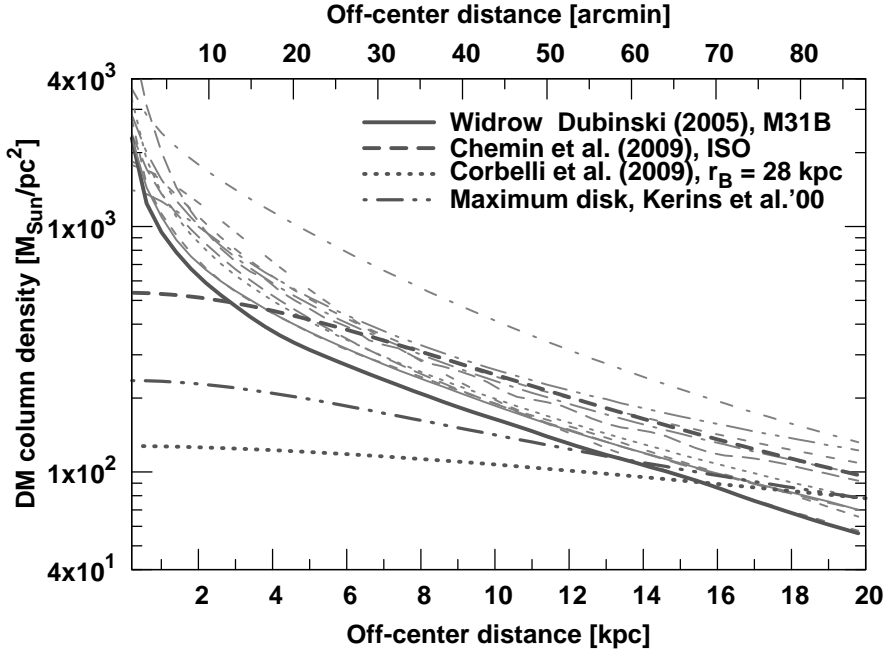
Figure 4.2: Dark matter column density of M31 as a function of off-center distance. The thin grey lines represent models from [194, 197, 285, 298, 322, 341] analyzed in [230]. The thick solid line represents the most conservative model M31B of [197]. The model of [12] (thick dashed line), the maximum disk model of [341] (thic dashed double-dotted line) and the "minimal" model ofk [11] (thick dotted line) (see text) are shown for comparison.

and new data on mass distribution of M31 became available.[5] In [12] modeling of HI rotation curve between ~ 0.3 kpc and 38 kpc was performed. [12] used *R-band* photometric information [343, 344] to determine the relative contribution of the stellar disk and the bulge. Based on this information and taking into account foreground and internal extinction/reddening effects [see section 8.2.2 in 12, for details] they determined mass-to-light ratio, using stellar population synthesis models [345] $\Upsilon_{disk} \simeq 1.7\Upsilon_{\odot}$ (in agreement with those of [197, 285]). Aiming to reproduce the data in the inner several kpc, they explored different disk-bulge decompositions with two values of the bulge's mass-to-light ratio $\Upsilon_{bulge} \simeq 0.8\Upsilon_{\odot}$ and $\Upsilon_{bulge} \simeq 2.2\Upsilon_{\odot}$ (all mass-

---

[5]We thank A. Kusenko and M. Loewenstein in drawing our attention to these works [342].

to-light ratios are in solar units). [12] analyzed several dark matter density profiles (NFW, Einasto, cored profile). According to their 6 best-fit models (3 dark matter density profiles times two choices of mass-to-light ratio) the dark matter column density in the Andromeda galaxy is higher than the one, adapted in [230] (model M31B) everywhere but inside the inner 1 kpc (see thick dashed line on Fig. 4.2).

[11] used circular velocity data, inferred from the HI rotation curves, also extending out to $\sim 37 \, \text{kpc}$. The authors exclude from the analysis the inner 8 kpc, noticing the presence of structures in the inner region (such as a bar), associated with non-circular motions. [11] also use optical data of [344] and determine an upper and lower bounds on the disk mass-to-light ratio using the same models [345, 346] as [12]. They obtain possible range of values of the *B-band* mass-to-light ratio $2.5\Upsilon_\odot \leq \Upsilon_{\text{disk}} \leq 8\Upsilon_\odot$. These values do not take into account corrections for the internal extinction.[6] [11] fit the values of Υ_{disk} rather than fixing it to a theoretically preferred value. The mass-to-light ratio of the disk of a spiral galaxy is known to be poorly constrained in such a procedure since the contributions of the disk and dark matter halo are similar (see e.g. discussions in [12, 197]). [11] analyzed variety of dark matter models and mass-to-light ratios, providing good fit to the data. The mass model that maximizes the contribution of the stellar disk ($\Upsilon_{\text{disk}} = 8$) has the core of the Burkert profile [306] $r_B = 28 \, \text{kpc}$ (if one imposes additional constraint on the total mass of M31 within several hundred kpc). The dark matter column density remains in this model remains essentially flat from the distance $\sim r_B$ inward (see Fig. 4.2). Notice, that the "maximum disk" fitting of [341] (blue dashed double-dotted line on Fig. 4.2) has higher dark matter content. Therefore in this work we will adopt the Burkert dark matter model of [11] as a *minimal* possible amount of dark matter, consistent with the rotation curve data on M31. The corresponding dark matter column density is factor 2–3 lower than the one given by the previously adapted model M31B in the inner 10 kpc. In what follows we will provide the restrictions for both M31B (as the *most conservative* among physically motivated models of dark matter distribution in M31) and Burkert model of [11].

---

[6]The correction for foreground extinction was taken into account in [11], using the results of [347]. The uniform disk extinction was not applied (which explains high values of Υ_{disk}). The authors of [11] had chosen not to include any uniform extinction corrections due to the presence of a gradient of B-R index (E. Corbelli, private communication).

ObsID	Cleaned exposure [ks] (MOS1 / MOS2 / PN)	FoV [arcmin^2] (MOS1 / MOS2 / PN)
0109270101	16.8 / 16.7 / 15.3	335.4/ 336.0 / 283.6
0112570101	39.8 / 40.0 / 36.0	332.9/ 333.1 / 285.9
0112570401	29.8 / 29.9 / 23.5	335.6/ 336.1 / 289.5

Table 4.2: Cleaned exposures and field-of-view after the removal of point sources and out-of-time events (calculated using BACKSCAL keyword) of three `M31on` observations.

4.1.3.2 M31 central part

Three observations of the central part of M31 (see Table 4.2 for details) were used in [230] to search for a dark matter decay signal. After the removal of bright point sources, the diffuse spectrum was extracted from a ring with inner and outer radii $5'$ and $13'$, centered on M31[7] (see [230] for details, where this region was referred to as `ring5-13`). We call these three observations collectively `M31on` in what follows. The baseline `powerlaw` model has the total $\chi^2 = 1328$ for 1363 d.o.f. (reduced $\chi^2 = 0.974$).

Below, we estimate the improvement of the signal-to-noise ratio (4.1), assuming the dark matter origin of [316] spectral feature. The average dark matter column density in the model M31B of [197]) is $\mathcal{S}_{\mathrm{M31on}} = 606\,M_\odot\,\mathrm{pc}^{-2}$. The dark matter column density from the Milky Way halo in this direction is $74.1\,M_\odot\,\mathrm{pc}^{-2}$.

The ratio of $t_{\exp} \times \Omega_{\mathrm{fov}} \times A_{\mathrm{eff}}$ of all observations of `M31on` (Table 4.2) and the [316] observation is 12.9. Thus one expects the following improvement of the S/N ratio:

$$\frac{(S/N)_{\mathrm{M31on}}}{(S/N)_{\mathrm{W1}}} = \frac{606 + 74.1}{208.5 + 73.9}\sqrt{12.90} \approx 8.65 \;, \tag{4.3}$$

i.e. the $\sim 2.5\sigma$ signal of [316] should become a prominent feature (formally about $\sim 21.6\sigma$ above the background) for the `M31on` observations. As described in Section 4.1.2 we add to the baseline powerlaw spectrum a narrow Gaussian line with the normalization fixed at $F_{\mathrm{M31on}} = \frac{606+74.1}{208.5+73.9}F_{\mathrm{W1}} \approx 1.08 \times 10^{-7}$ photons cm^{-2} s^{-1} arcmin^{-2}. The quality of fit becomes significantly worse (see Fig. 4.3). The increase of the total χ^2 due to the adding of

---

[7]We adopt the distance to M31 $D_L = 784$ kpc [348] (at this distance $1'$ corresponds to 0.23 kpc).

a line is equal to $(23.2)^2$, $(22.9)^2$ and $(22.2)^2$ for 1σ, 2σ and 3σ intervals with respect to the central respectively.

In addition to the `M31on` observations, we processed an *XMM-Newton* observation `0402560301`, positioned $\approx 22'$ off-center M31 (RA = 00h40m47.64s, DEC = +41d18m46.3s) – `M31off` observation, see Table 4.3. We collected the spectra from the central $13'$ circle. Several point sources were manually excluded from the source spectra. The rest of data reduction is described in the Section 4.1.3.2. The fit by the `powerlaw` model is excellent, the total χ^2 equals to 895 for 997 d.o.f. (the reduced $\chi^2 = 0.898$). Using the dark matter estimate based on the model M31B we find that the average dark matter column density for the `M31off` $S_{\text{M31off}} = 388.6 M_\odot \, \text{pc}^{-2}$ plus the Milky Way halo contribution $74.3 M_\odot \, \text{pc}^{-2}$. The estimate of the line significance is similar to the previous Section and gives

$$\frac{(S/N)_{\text{M31off}}}{(S/N)_{\text{W1}}} = \frac{388.6 + 74.3}{208.5 + 73.9}\sqrt{8.76} \approx 4.85 \tag{4.4}$$

and therefore, under the assumption of dark matter nature of the feature of [316], one would expect $\sim 12.1\sigma$ detection. After that, we add a narrow line with the normalization $F_{\text{M31off}} \approx 7.37 \times 10^{-8}$ photons $\text{cm}^{-2} \, \text{s}^{-1} \, \text{arcmin}^{-2}$ and perform the procedure, described in Section 4.1.2. The observation `M31off` rules out the dark matter decay line origin of the [316] feature with high significance (see Fig. 4.4): the increase of χ^2 due to the addition of this line has the minimum value $\Delta\chi^2 \simeq (10.4)^2$ at 2.44 keV, which is within 1σ interval of the quoted central value of the [316] feature.

We also perform the analysis, adding a line, whose flux is determined according to the dark matter density estimates based on the model of [11], that we consider to be a minimal dark matter model for M31 (as discussed in 4.1.3.1). For this model the column density in the central 1–3 kpc decreases by a factor ~ 3.4 as compared with the value, based on M31B. [342] claimed that in this case the [316] line becomes consistent with the `M31on` observations. However, our analysis shows that the total χ^2 *increases*, when adding the corresponding line to the model, by $(5.7)^2$ for 3σ variation of the position of the line. The corresponding increase of total χ^2 for `M31off` region is $(2.0)^2$. Combining `M31on` and `M31off` observations, one obtains $(6.2)^2$ increase of the total χ^2.

We conclude therefore that despite the uncertainties in dark matter modeling, the analysis of diffuse emission from the central part of M31 (1–8 kpc
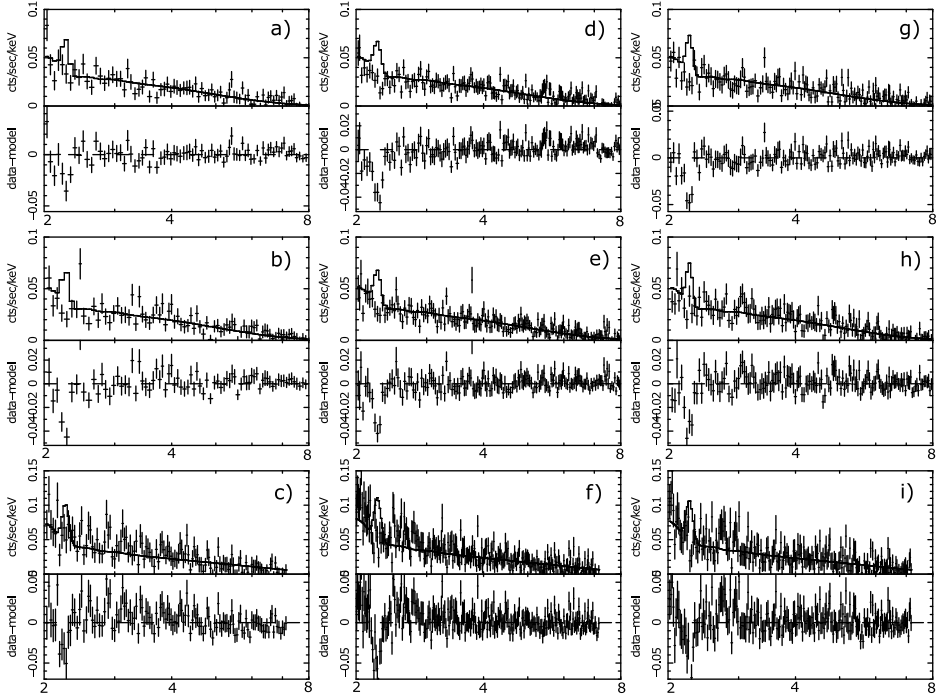
Figure 4.3: Spectra of three *XMM-Newton* observations of M31 (`M31on`, Sec. 4.1.3.2). The Gaussian line, obtained by proper scaling of the result of [316] is also shown. The top row is for MOS1, the middle row – for MOS2, and the bottom row for PN cameras. The spectra in the left column are for the observation `0109270101`, the middle column – `0112570101` and the right column – for `0112570401`. The error bars include 5% of the model flux as an additional systematic error. For all these spectra combined together, the χ^2 increases by *at least* 22.2^2, when adding a narrow Gaussian line in any position between $2.3\,\mathrm{keV}$ and $2.72\,\mathrm{keV}$ (see text).

off the center), as measured by *XMM-Newton*, disfavors the hypothesis that the spectral feature, observed in Willman 1, is due to decaying dark matter. Nevertheless, to strengthen this conclusion further we analyzed available *XMM-Newton* observations of M31 in the region 10–$20\,\mathrm{kpc}$ off-center, where the uncertainties in the mass modeling of M31 reduce significantly as compared with the central $5 - 8\,\mathrm{kpc}$ (c.f. [11, 12], see also Section 4.1.3.1, in particular Fig. 4.2).

ObsID	Cleaned exposure [ks] (MOS1 / MOS2 / PN)	FoV [arcmin^2] (MOS1 / MOS2 / PN)
0402560301	41.9 / 42.2 / 35.2	405.6/ 495.4 / 433.3

Table 4.3: Cleaned exposures and field-of-view (calculated using BACKSCAL keyword) of the observation M31off (obsID 0402560301). The significant difference in FoVs between MOS1 and MOS2 cameras is due to the loss CCD6 in MOS1 camera.
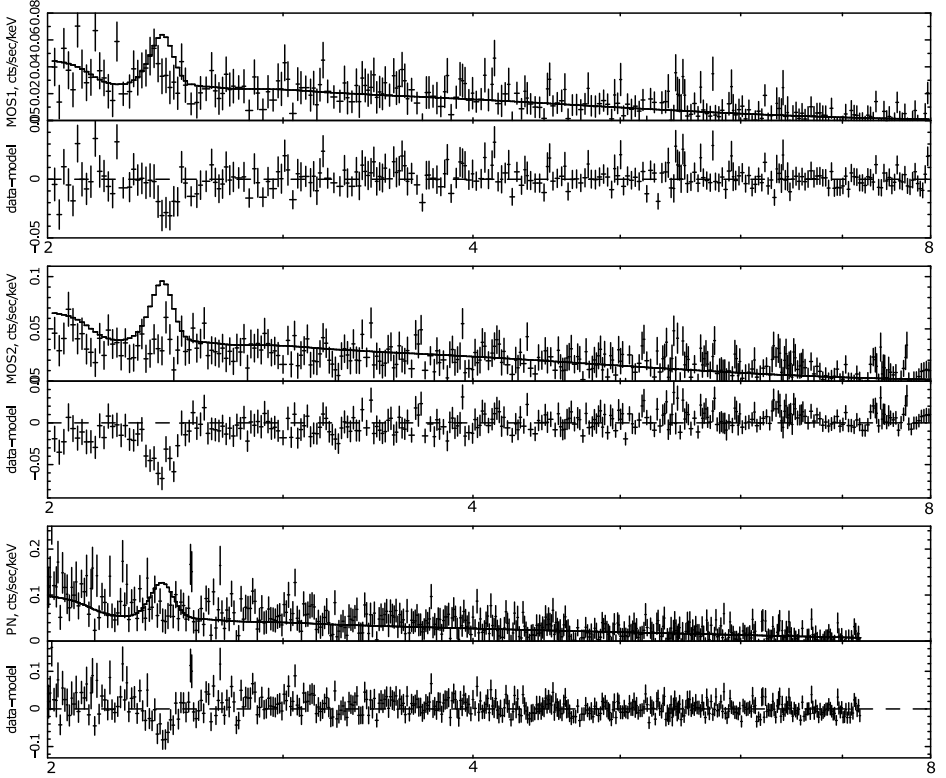

Figure 4.4: The spectra of off-center M31 observation 0402560301 (M31off, Sec.4.1.3.3). The decaying dark matter signal, obtained by proper scaling of the result of [316] is also shown. The error bars include 5% of the model flux as an additional systematic error. Fitting these spectra together excludes the properly scaled line of [316], at the level of at least 10.4σ (see text).

ObsID	Cleaned exposure [ks] (MOS1 / MOS2 / PN)	FoV [arcmin^2] (MOS1 / MOS2 / PN)
0511380101	44.3 / 44.5 / 37.6	356.2 / 400.4 / 333.3
0109270401	38.5 / 38.4 / 33.5	387.8 / 384.1 / 366.7
0505760401	26.0 / 26.0 / 21.7	330.5 / 374.1 / 325.0
0505760501	23.8 / 23.8 / 19.8	344.8 / 395.2 / 313.2
0402561301	22.7 / 22.7 / 20.1	367.2 / 419.5 / 382.6
0402561401	39.3 / 39.3 / 33.7	349.9 / 408.3 / 343.6
0402560801	42.6 / 42.6 / 36.6	373.6 / 435.8 / 393.7
0402561501	38.5 / 38.5 / 34.0	369.3 / 421.0 / 407.5
0109270301	24.4 / 24.6 / 22.2	443.4 / 439.6 / 405.0

Table 4.4: Cleaned exposures and field-of-view after the removal of point sources and out-of-time events (calculated using BACKSCAL keyword) of nine M31 observations off-set by more than 10 kpc from the center (`M31out` observations).

4.1.3.3   M31 off-center (10-20 kpc)

We selected 9 observations with MOS cleaned exposure greater than 20 ks (Table 4.4). The total exposure of these observations is about 300 ks. Based on the statistics of these observations one would expect a detection of the signal of [316] with the significance 12.1σ (for M31B) and 11.2σ (for [11]). The fit to the baseline model is very good, giving total χ^2 equal to 5931 for 5883 d.o.f. (the reduced $\chi^2 = 1.008$). However, adding the properly res-caled line significantly reduced the fit quality, increasing the total χ^2 by $(12.0)^2/(10.7)^2/(10.7)^2$ when varying line position within 1σ, 2σ and 3σ inter-vals (using M31B model) and by $(11.7)^2$, $(10.7)^2$ and $(10.6)^2$ for 1σ, 2σ and 3σ intervals (using the model of [11], which gives dark matter column density in `M31out` about $160 - 180 M_\odot \, \mathrm{pc}^{-2}$ (including Milky Way contribution), see Fig. 4.2).

4.1.3.4   Combined exclusion from M31

Finally, performing a combined fit to all 13 observations of M31 (`M31`, `M31off`, `M31out`) we obtain the exclusion of more than 26σ (using the dark matter model M31B of [197]) and more than 13σ for the minimal dark matter model of [11]. As described in Section 4.1.2, in deriving these results we allowed the normalization of the baseline `powerlaw` model to vary independently

for each camera, observing the same spatial region, added additional 5% of the model flux as a systematic uncertainty and allowed the position of the narrow line to vary within $2.3 - 2.72\,\mathrm{keV}$ interval.

4.1.4 Fornax dwarf spheroidal galaxy and Willman 1

We use dark matter distributions in Fornax dwarf spheroidal galaxy and Willman 1 presented in [323]. In this paper, it is shown that the mass distribution in Willman 1, as well as its galactic status (dwarf spheroidal galaxy vs metal-poor globular cluster) remain uncertain, mostly due to extreme smallness of available kinematic data. For example, [316] have used the dark matter distribution from [191] who used velocities of only 47 stars. In [323], the authors used even smaller published sample of 14 stars which does not allow to significantly constrain the dark matter distribution. For example, dark matter distribution in Fornax and Sculptor dwarf spheroidal galaxies, the brightest and most well-studied dSph satellites of the Milky Way, the availability of large kinematic data set of ~ 2600 and ~ 1400 members, respectively [349], allows to place relatively tight constraints on the dark-matter column densities with the help of Monte Carlo Markov chain analysis procedure of [196]. To characterize the dark matter halos of dSphs, [323] adopt the general dark matter halo model of [196], with density profile given by

$$\rho(r) = \rho_s \left(\frac{r}{r_s} \right)^{-\gamma} \left[1 + \left(\frac{r}{r_s} \right)^{\alpha} \right]^{\frac{\gamma-3}{\alpha}}, \tag{4.5}$$

where the parameter α controls the sharpness of the transition from inner slope $\lim_{r\to 0} d\ln(\rho)/d\ln(r) \propto -\gamma$ to outer slope $\lim_{r\to\infty} d\ln(\rho)/d\ln(r) \propto -3$. This model includes as special cases both *cored* ($\alpha = 1, \gamma = 0$) and NFW [305] ($\alpha = \gamma = 1$) profiles. The results are shown in Fig. 4.5 and have been used for the subsequent analysis.

4.1.4.1 *XMM-Newton* observation of Fornax dSph

Fornax is one of the most deeply observed dSphs in X-ray wavelengths. We have processed the 100 ks *XMM-Newton* observation (ObsID `0302500101`) of the central part of Fornax dSph. The data analysis is described in the Section 4.1.2. In each camera, we extract signal from the $14'$ circle, centered on the Fornax dSph. The cleaned exposure and corresponding fields of view
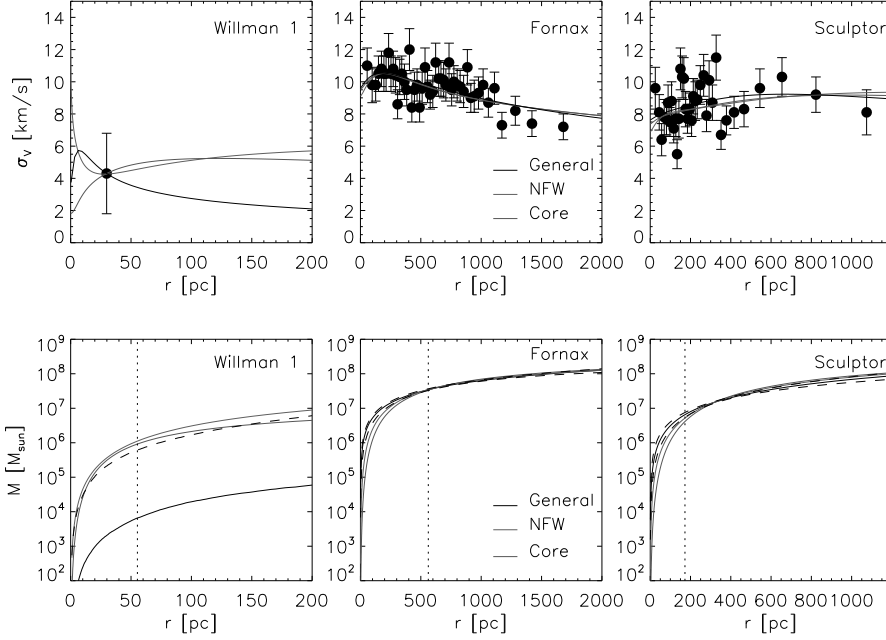
Figure 4.5: Dark matter mass modeling in Fornax and Willman 1 from [323]. Top panels display empirical velocity dispersion profiles as calculated by [196] for Fornax, Sculptor and from the Willman 1 data of [350] (for Willman 1, the small published sample of 14 stars allows for only a single bin). Overplotted are the median profiles obtained from the Monte-Carlo Markov chain analysis described by [196], using the general dark matter halo model (4.5), as well as the best-fitting NFW and cored halo models. Bottom panels indicate the corresponding spherically-enclosed mass profiles. In the bottom panels, dashed lines enclose the central 68% of accepted general models (for Willman 1, the lower bound falls outside the plotting window). Vertical dotted lines indicate the outer radius of the field of view of the X-ray observations ($14'$ for Fornax, $7.5'$ for Sculptor and $5'$ for Willman 1).

XMM-Newton ObsID	Cleaned exposure [ks] (MOS1 / MOS2 / PN)	FoV [arcmin^2] (MOS1 / MOS2 / PN)
0302500101	53.8 / 53.9 / 48.2	459.1 / 548.5 / 424.9

Table 4.5: Cleaned exposures of the *XMM-Newton* observation of Fornax dSph

(calculated using the BACKSCAL keyword) for all three cameras (after subtraction of CCD gaps, out-of-time strings in PN camera and CCD 6 in MOS1 camera) are shown in Table 4.5. Based on the dark matter estimates, presented in [323] we expect the following improvement in S/N ratio

$$\frac{(S/N)_{\mathrm{Forn}}}{(S/N)_{\mathrm{W1}}} = \frac{54.4 + 83.2}{208.5 + 73.9}\sqrt{12.12} \approx 1.70 \tag{4.6}$$

i.e. we expect a $\sim 4.2\sigma$ signal from Fornax, assuming dark matter decay line origin of the [316] feature.

The fit to the baseline model is very good, $\chi^2 = 955$ for 983 d.o.f. (reduced $\chi^2 = 0.972$). Note that the parameters are consistent with those of extragalactic diffuse X-ray background as it should be for the dwarf spheroidal galaxy where we do not expect any diffuse emission at energies above $2\,\mathrm{keV}$ [see also 223, 228, 318, 319, 351].

After adding a narrow line with the normalization $F_{\mathrm{Forn}} \approx 2.19 \times 10^{-8}$ photons cm^{-2} s^{-1} arcmin^{-2}, the χ^2 *increases*, the minimal increase is equal to $(5.1)^2$, $(4.2)^2$ and $(3.3\sigma)^2$ for a position of the line within 1σ, 2σ and 3σ intervals from [316] feature, respectively (after adding 5% of model flux as a systematic error). We see that adding a properly scaled Gaussian line worsens χ^2 by at least $\sim 3.3\sigma$ (instead of expected *improvement* of the quality of fit by a factor of about 16 if the [316] feature were the dark matter decay line), see Fig. 4.6 for details.

The combination of all *XMM-Newton* observations used in this work (M31on, M31off, M31out and Fornax) provide a minimum of 26.7σ exclusion at 2.35 keV (which falls into the 3σ energy range for the [316] spectral features), after adding a 5% systematic error. Within 1σ and 2σ energy intervals, the minimal increase of χ^2 is 29.0^2 and 27.3^2, correspondingly. Therefore, one can exclude the dark matter origin of the [316] spectral feature by 26σ. This exclusion is produced by using the most conservative dark matter model M31B of [197]. Using the minimal dark matter model of [11], one can exclude the [316] feature at the level more than 14σ.
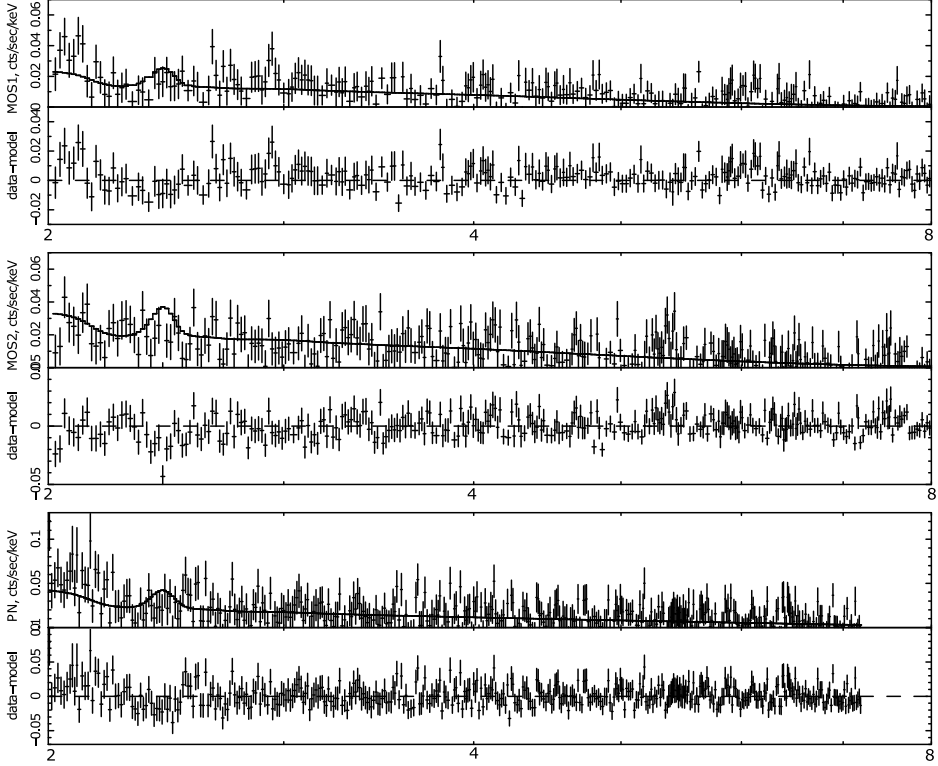
Figure 4.6: The spectra of the *XMM-Newton* observation `0302500101`, Sec. 4.1.4.1. The error bars include 5% of the model flux as an additional systematic error. Fitting these spectra together excludes the properly scaled [316] line at the level of at least 2σ (3.3σ if one restricts the position of the line to the interval $2.30 - 2.72$ keV) instead of expected improving of the quality of fit by about 4σ (if the line were of the dark matter origin).

Regions	PL index, best-fit	PL norm. best-fit	Line position	Line signif.	Line flux best-fit value	Line flux 3σ *upper* bound
M31on	1.32	1.66/1.82/2.39	2.55	1.7σ	7.35×10^{-9}	2.09×10^{-8}
M31off	1.42	1.51/1.19/2.22	2.47	2.3σ	6.69×10^{-9}	3.10×10^{-8}
M31out	...	.../.../...	2.52	1.6σ	3.76×10^{-9}	1.16×10^{-8}
Fornax	1.37	0.79/0.59/0.70	2.19	2.6σ	9.63×10^{-9}	2.11×10^{-8}

Table 4.6: Parameters of the best-fit `powerlaw` components (assuming the `powerlaw+gauss` model) and of the maximally allowed flux in the narrow Gaussian line in the interval $2.1 - 2.8$ keV. The normalization of the `powerlaw` is given in 10^{-6} photons cm^{-2} s^{-1} arcmin^{-2} keV^{-1}, line position – in keV, fluxes of `gaussian` – in photons cm^{-2} s^{-1} arcmin^{-2} keV^{-1}. The slight difference between these values and those of Table 4.1 is due to the presence of `gaussian` component and the proportionality of `powerlaw` normalization to field-of-view solid angle (for `M31on`); for each observation, the corresponding parameters coincide within 90% confidence range. The values of best-fit `powerlaw` parameters for `M31out` are not shown because they are different for different observations (see Table 4.1).

4.1.5 On a possible origin of a 2.5 keV feature

We provide more than 80 times improvement of statistics of observations, as compared to [316] (factor ~ 5 times larger total exposure time and factor ~ 4 improvement in both the effective area and the field-of-view). Even under the most conservative assumption about the dark matter column density such an improvement should have led to an about 14σ detection of the dark matter decay line. In our analysis no significant lines in the position, predicted by [316] were found. However, in the *XMM-Newton* observations that we processed there are several spectral features in the range $2 - 3$ keV (see Table 4.6). This is not surprising, as the *XMM-Newton* gold-coated mirrors have Au absorption edge at ~ 2.21 keV [339, 340] and therefore their effective areas possess several prominent features in the energy range $2 - 3$ keV. According to *XMM-Newton* calibration report [339, 340], there is about 5% uncertainty at the modeling of the effective area of both MOS and PN cameras at these energies. These uncertainties in the effective area can lead to artificial spectral features due to the interaction of the satellite with cosmic rays [352]. In particular, the solar protons with energies of few hundreds keV can be interpreted as X-ray photons (so called *soft proton flares*). The interaction efficiency of solar protons with the instrument is known to be totally different from that of real photons [329]. In particular, their flux is not af-

fected by the Au edge of the *XMM-Newton* mirrors. According to [329], the spectrum of soft proton flares for EPIC cameras is well described by the *unfolded* (i.e. assuming that the instrument's response is energy-independent) broken powerlaw model with the break energy around ~ 3.2 keV, `bknpow/b` in `XSPEC v.11`. Therefore, modeling the spectrum that is significantly contaminated with soft proton flares in a standard way (i.e. by using *folded* `powerlaw` model) will produce artificial residual excess at energies of sharp decreases of the instrument's effective area.

In our data analysis we performed both the standard flare screening [325–327] that uses the inspection of high-energy (10–15 keV) light curve and an additional soft proton flare cleaning. As found by [353], it is possible to screen out the remaining flares, e.g. by the visual inspection of the cleaned lightcurve at low and intermediate energies. To provide the additional cleaning after the rejection of proton flares at high energies, we followed the procedure of [329, 330], leaving only the time intervals, where the total count rate differs from its mean value by less than 2σ.

To test the possible instrumental origin of the features, discussed in this Section, we first performed only a high-energy light curve cleaning [325–327] and determined the maximally allowed flux in a narrow line in the energy interval of interest. After that we performed an additional soft proton cleaning. This procedure improved the quality of fit. The significance contours of the resulting "line" (for `M31out` region) are shown on the left panel in Fig. 4.7. In deriving these limits we allowed both the parameters of the background, the position of the line and its total normalization to vary (the latter from negative values). Finally, we added an unfolded broken power-law component `bknpow/b` to model a contribution of remaining soft proton flares (see e.g. [329]). The break energy was fixed as 3.2 keV so no degeneracy with the parameters of the `gaussian` is expected. The `bknpow/b` power-law indices at low and high energies were fixed to be the same for different cameras observing the same spatial region. further improved the quality of fit and made the line detection totally insignificant (see right Fig. 4.7 for details). Our analysis clearly suggests the instrumental origin of the line-like features at the energy range 2.1–2.8 keV.

As a final note, we should emphasize that the *Chandra* ACIS instrument used in [316] has the Ir absorption edges near 2.11 and 2.55 keV (see [354] for additional discussion). They also report negative result of searching for
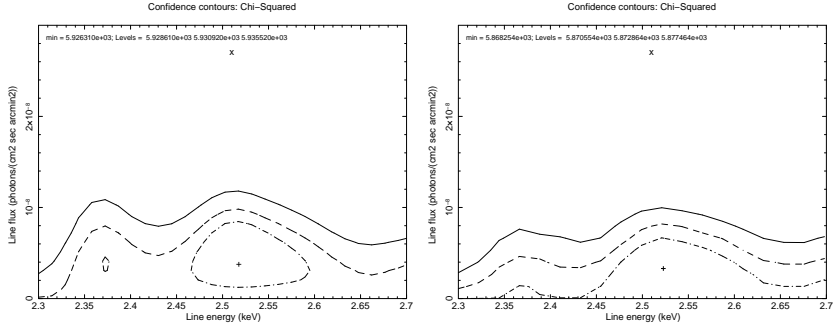
Figure 4.7: *Left:* $\Delta\chi^2 = 2.3$ (dashed-dotted), 4.61 (dashed) and 9.21 (solid) contours (corresponding to 68%, 90% and 99% confidence intervals) for a thin `gaussian` line allowed by the joint fit of `M31out` spectra used in this work. The resulting line normalizations are shown for an averaged dark matter column density in the `M31out` region (about $170 M_\odot\,\mathrm{pc}^{-2}$, including the Milky Way contribution). The rescaled [316] line is marked with a cross x; its normalization is therefore $4.50 \times 10^{-8} \times \frac{170}{208.5+73.9} = 2.71 \times 10^{-8}\mathrm{photons\ cm}^{-2}\ \mathrm{sec\ arcmin}^{-2}$. It is clearly seen that the hypothesis of dark matter origin for a [316] line-like feature is excluded at extremely high significance, corresponding to more than $\approx 10\sigma$ (see text). *Right:* The same as in the left figure but with an addition of a `bknpow/b` component to model the contribution of the remaining soft proton contamination (see text). The break energy is fixed as 3.2 keV so no degeneracy with the parameters of the `gaussian` is expected. The `bknpow/b` powerlaw indices at low and high energies are fixed to be the same for different cameras observing the same spatial region. The line significance drops below 1σ in this case.

the [316] feature, in agreement with our findings.

4.1.6 Conclusion

To summarize, by comparing the strength and position of the feature found by Loewenstein & Kusenko with observations of several dark matter-dominated objects (M31, Fornax and Sculptor[8] dSphs) we found that the hypothesis of dark matter origin of [316] is excluded with the combined significance exceeding 14σ even under the most conservative assumptions. This is possible because of the large increase of the statistics in our observations as compared with the observation used in [316].

---

[8]Non-detection of $\sim$2.5 keV line in *Chandra* observations of Sculptor dwarf spheroidal galaxy by [323] further strengthens our result.

4.2 Summary of existing X-ray bounds on decaying dark matter parameters

Table 4.7 summarizes existing works that put bounds on decaying dark matter from observations of individual objects. In this Table, we do not discuss the claim [355] that the intensity of the Fe XXVI Lyman-γ line at $8.7\,\mathrm{keV}$, observed in [356] cannot be explained by standard ionization and recombination processes, and that the dark matter decay may be a possible explanation of this apparent excess. Spectral resolution of current missions does not allow to reach any conclusion. However, barring an *exact* coincidence between energy of decay photon and Fe XXVI Lyman-γ, this claim may be tested with the new missions, discussed in Chapter 6.

4.3 Strategy of further searches for decaying dark matter

Our results (Chapter 3, in particular Section 3.4) allow us to identify the best observational targets and the strategy of searches for decaying dark matter.

The objects with the largest dark matter decay signal turn out to be the nearby galaxy clusters. However, the detection of the dark matter decay line from galaxy clusters in X-rays is complicated by the fact that most of them show strong emission precisely in keV range.[9] Indeed, the virial theorem immediately tells us that the temperature of the intercluster medium is

$$T_{\mathrm{gas}} \sim G_N\, m_p\, \mathcal{R}\rho_* r_*^2, \tag{4.7}$$

where ρ_*, r_* are characteristic density and size (see Section 3.1), $\mathcal{R}$ is a typical overdensity in objects of a given type, m_p is the proton mass. For galaxy clusters the overdensity $\mathcal{R} \sim 10^3$ and size $r_* \sim 1\,\mathrm{Mpc}$, the temperature T_{gas} is always in the keV range, which makes it hard to detect a dark matter decay line against a strong X-ray continuum.

The optimal targets for detection the dark matter line become X-ray faint objects, such as dwarf spheroidal galaxies which do not contain any X-ray

---

[9]When searching for decaying dark matter signatures in other energy ranges, e.g. in the GeV range, galaxy clusters become the best targets, see e.g. [364].

Reference	Object	Instrument	Cleaned exp, ks
[221]	Diffuse X-ray background	HEAO-1, *XMM-Newton*	224, 1450
[222]	Coma & Virgo galaxy clusters	*XMM-Newton*	20, 40
[223]	Large Magellanic Cloud	*XMM-Newton*	20
[224]	Milky Way halo	*Chandra*/ACIS-S3	Not specified
[225][a]	M31 (central $5'$)	*XMM-Newton*	35
[357]	Abell 520 galaxy cluster	*Chandra*/ACIS-S3	67
[228]	Milky Way halo, Ursa Minor dSph	*XMM-Newton*	547, 7
[358]	Milky Way halo	*Chandra*/ACIS	1500
[226]	Galaxy cluster 1E 0657-56 ("Bullet")	*Chandra*/ACIS-I	450
[229]	Milky Way halo	X-ray microcalorimeter	0.1
[359][b]	Milky Way halo	INTEGRAL/SPI	5500
[230]	M31 (central $5-13'$)	*XMM-Newton*/EPIC	130
[231][b]	Milky Way halo	INTEGRAL/SPI	12200
[318]	Ursa Minor	*Suzaku*/XIS	70
[319]	Draco dSph	*Chandra*/ACIS-S	32
[316][c]	Willman 1	*Chandra*/ACIS-I	100
[323][d]	M31, Fornax, Sculptor	*XMM-Newton*/EPIC , *Chandra*/ACIS	400, 50, 162
[354][e]	Willman 1	*Chandra*/ACIS-I	100
[360]	Segue 1	Swift/XRT	5
[361]	M33	*XMM-Newton*/EPIC	20-30
[362]	M31 ($12-28'$ off-center)	*Chandra*/ACIS-I	53
[363]	Willman 1	*XMM-Newton*	60
[71]	Ursa Minor, Draco	*Suzaku*/XIS	200, 200

Table 4.7: Summary of existing X-ray observations of different objects performed by different groups.

[a] Mistakes on calculating the bound, see discussion in [230].

[b] INTEGRAL/SPI is sensitive at 20 keV–7 MeV.

[c] Claimed presence of 2.5 keV feature.

[d] Did not put any bounds, only checked of the origin of 2.5 keV feature.

[e] Re-analyzed the same observation of Willman 1, did not find 2.5 keV feature.

gas [223]. However archival observations of dwarf spheroidal galaxies have rather short exposure.

Objects with comparable column density and X-ray quiet (at least in energies above 1–2 keV) are the *nearby spiral galaxies*. Of these objects the Milky Way (including LMC and SMC satellites) and Andromeda galaxy had been observed for the longest (combined) time. In Fig. 2.2 it is shown that the strongest bounds on parameters of decaying dark matter particles come from either Milky Way halo [228] or the central part of the Andromeda galaxy [230].

The strongest existing bounds (those of [223, 228, 230]) used the X-ray observations of LMC, Milky Way and Andromeda galaxy whose effective exposure was below 200 ksec (see Table 4.7)[10]

In this situation the current generation of X-ray telescopes there are two possible ways to further improve the existing bounds and probe the theoretically interesting regions of particle physics models:

1. Deep (few mega-seconds)[11] observations of the most X-ray quiet objects. "*Classical*" dwarf spheroidal galaxies (Ursa Minor, Draco, Sculptor, Fornax), where the dark matter content can be determined robustly are the preferred targets. The problem with this approach is the limited visibility of some of these objects and large investment (about 10%) of the annual observational time of the satellite (total observational time available each year for *XMM-Newton* and *Chandra* satellites is about half of the calendar year, i.e. 14–15 Msec). Allocating time for such an observation in the absence of a candidate line is hardly possible. On the other hand, observations of these objects would provide an important confirmation of the signal, detected with some other means.

2. Total exposure of all observations of dark matter-dominated objects with the X-ray satellites is several orders of magnitude longer than any possible single observation. Therefore a possible way to advance with the existing X-ray instruments is *to combine a large number* of X-ray observations of different dark matter-dominated objects. The idea is that the spectral position of the dark matter decay line is the same for

---

[10]For Milky Way halo [228], total exposure of the combined blank sky dataset was ~ 547 ks, but due to subtraction of instrumental background with ~ 145 ks exposure, the errorbars of the subtracted spectrum were mainly defined by the exposure of the background.

[11]Even longer exposure will not improve the situation, as the error bars will begin to be dominated by systematic uncertainties, see the next Chapter for detailed discussion.

all these observations, while the astrophysical backgrounds in the combined spectrum would "average out", producing a smooth continuum against which a small line would become visible. Naively, such a data-set, uniformly processed, should allow to improve the existing bounds by at least an order of magnitude *and* study spatial dependence of each candidate line.

3. Finally, drastic improvement in the decaying dark matter search is possible with a *new generation of spectrometers*, having large field of view and energy resolution close to several eV [75, 229, 365, 366]. In Chapter 4, we discuss this possibility in more details.